Physics-informed background-oriented schlieren of turbulent underexpanded jets

Joseph P. Molnar, Samuel J. Grauer, Olivier Léon, David Donjat, François Nicolas

Physics-Informed Background-Oriented Schlieren of Turbulent Underexpanded Jets

Joseph P. Molnar* and Samuel J. Grauer†
Pennsylvania State University, University Park, Pennsylvania 16802

Olivier Léon‡ and David Donjat§
ONERA/DMPE, Université de Toulouse, 31055 Toulouse, France

François Nicolas¶
ONERA/DAAA, Université Paris-Saclay, 92190 Meudon, France

Background-oriented schlieren (BOS) is an imaging technique that can be used to characterize the density field in a compressible flow. This information is often employed to assess shock formations and predict aerodynamic performance in high-speed ground tests. However, measurements in ground test facilities are subject to large uncertainties due to limitations on optical access, short exposure times/high signal-to-noise ratios, and intense vibrations that lead to calibration drift. Further, it can be difficult to interpret scalar measurements in a complex flow. Data assimilation (DA) can ameliorate these issues by optimally combining measurement information with the relevant governing equations. Doing so enhances the accuracy of parameter estimates and provides access to latent (i.e., not directly measured) flow fields. We previously developed a DA algorithm for BOS to recover the density, velocity, and total energy fields of compressible inviscid flows from noisy experimental images. Here, we refine and deploy our "physics-informed BOS" technique using the compressible RANS equations, testing the method on a suite of turbulent underexpanded jets. The resulting mean fields agree with simulations and measurements reported in the literature.

Nomenclature

$\mathbf{b}$	=	image difference data vector, a.u.
C_{sys}	=	imaging system constant, px m^3 kg^{-1}
D	=	diameter, m
$\mathbf{D}$	=	deflectometry kernel
E	=	total energy, m^2 s^{-2}
f	=	focal length, mm
$f_\#$	=	f-number
I	=	intensity, a.u.
$\mathcal{L}$	=	objective loss component
L	=	domain length, m
M	=	Mach number
NPR	=	nozzle pressure ratio
p	=	pressure, kPa
Pr	=	Prandtl number
R	=	domain radius, m
R_{gas}	=	specific gas constant, J kg^{-1} K^{-1}
Re	=	Reynolds number

*Graduate Research Assistant, Department of Mechanical Engineering; jpm6128@psu.edu. Student Member AIAA.
†Assistant Professor, Department of Mechanical Engineering. Member AIAA.
‡Senior Research Scientist, Département Multi-Physique pour l'Énergétique.
§Senior Research Scientist, Département Multi-Physique pour l'Énergétique.
¶Senior Research Scientist, Département Aérodynamique, Aéroélasticité, Acoustique.

T = temperature, K
u = axial velocity, m s^{-1}
v = radial velocity, m s^{-1}
$\mathbf{X}$ = horizontal intensity gradient matrix
$\mathbf{Y}$ = vertical intensity gradient matrix
δ, $\boldsymbol{\delta}$ = deflection scalar and vector, px
ε = residual or error
γ = ratio of specific heats
μ = dynamic viscosity, kg m^{-1} s^{-1}
ρ, $\boldsymbol{\rho}$ = density scalar and vector, kg m^{-3}

Subscripts
α = directional component
amb = ambient conditions
cone = light cone
i = vector index
jet = fully expanded conditions
t, t = time label and partial derivative
tot = total conditions
T = turbulence model quantity (eddy)
x, x = x-direction label and partial derivative
y, y = y-direction label and partial derivative
0 = reference value (scale)

I. Introduction

Time-averaged flow fields are essential to the design of high-speed airborn vehicles, for instance, to predict coefficients of drag, the intensity of noise, propulsive power, and the like [1]. Computational fluid dynamics (CFD) has become essential to the design process, but the cost of resolving all the dynamically relevant scales remains prohibitive in the context of large-scale high-speed flows. Directly solving for the mean (or otherwise filtered) fields, e.g., using the Reynolds-averaged Navier–Stokes (RANS) equations, is still the method of choice when examining a large parameter space [2]. However, RANS and subgrid scale models tend to include empirical parameters and forms, especially to cope with extreme conditions, and may be laden with heuristics. Consequently, the ability to combine experimental measurements with the RANS equations in a streamlined solver – for the selection, calibration, and development of turbulence models – is an attractive prospect. Not only can such a "data assimilation" (DA) technique improve the fidelity of measurements, it can also enable the inference of latent fields and provide insight into the accuracy of turbulence and reduced-order models [3, 4].

Under- and overexpanded jets need to be better understood and modeled to support the design of next-generation supersonic aircraft. Imperfect expansion can lead to suboptimal thrust and shock–turbulence interactions that generate unwanted noise, which is often subject to regulatory restrictions [5]. These jets manifest when the dynamic pressure at the nozzle exit differs from the ambient pressure: a phenomenon that is often traced back to a poorly-designed nozzle or operating an aircraft outside of its design envelope. The goal of this work, therefore, is to develop a DA procedure that can shed light on the performance and noise characteristics of underexpanded jets by combining low-cost optical measurements of real-world representative jets with a numerical model that can account for turbulence.

Knife-edge schlieren has long been employed as a qualitative technique to visualize density field gradients in high-speed, buoyancy-driven, and thermally-driven flows [6]. Developments from the past several decades have accelerated the use of quantitative schlieren, and the advent of background-oriented schlieren (BOS) has been instrumental in this shift [7]. In BOS, one or more cameras is focused through the working fluid onto a background pattern; density gradients in the flow induce distortions in images of the pattern, which can be characterized by processing a pair of reference (flow-off) and distorted (flow-on) images with a computer vision algorithm. Distortions are characterized via so-called "deflections", i.e., the displacement of light rays in the plane of the background pattern, which may be tomographically reconstructed to recover the density field.

Deflection sensing and reconstruction are ill-posed inverse problems, meaning that additional information is required to obtain a physical solution [8]. For deflection sensing, an optical flow or cross-correlation algorithm is used to

process the image pairs [9]. For reconstruction, a wide variety of techniques has been developed to regularize the inversion, including iterative algorithms, classical regularization methods, and comprehensive DA solvers [10]. Iterative algorithms exhibit semi-convergence, meaning the solution diverges to a non-physical field unless stopped prematurely. Halting the solver can produce spatially-smooth fields, but doing so amounts to an ad-hoc method of regularization that is difficult to control and characterize [11]. Separately, classical regularization schemes add supplemental information to constrain the system, typically by promoting global [12] or piecewise [13] smoothness. Classical penalties are invariably inconsistent with the physics of compressible flows, which is a source of reconstruction artifacts. These limitations motivate a flexible, physics-informed DA scheme that can extract rich, quantitative information from BOS data.

This work demonstrates an approach to DA for BOS that optimally combines BOS measurements with the RANS equations to recover additional information about the target flow [14]. The method employs a physics-informed neural network (PINN) to represent the flow in functional form. We train the network to minimize a physics loss, based on the governing equations, as well as a data loss, which compares synthetic data outputted by the PINN to experimental measurements. In [14], we showed how this procedure, termed "physics-informed BOS", can recover the density, velocity, and total energy fields of inviscid Mach 2 flow over an axisymmetric cone-cylinder from a single pair of experimental images. Here, we apply physics-informed BOS to turbulent underexpanded jets using the compressible RANS equations instead of the compressible Euler equations.

Figure 1 depicts the BOS test rig, nozzle schematic, and computational domain of our experiments. This facility is owned and operated by the Office National d'Etudes et de Recherches Aérospatiales (ONERA) in Toulouse, France. The rig includes a camera, mounted to an outer frame and directed towards a background plate, itself printed with a semi-random dot pattern; the camera and background are positioned on either side of the flow domain. A series of high-speed jets are measured, reconstructed, and discussed. We introduce the working principles of physics-informed BOS in Sect. II. This leads into a discussion of our measurement scenario and validation efforts in Sect. III. Next, Sect. IV reviews some of the challenges associated with BOS and assesses an imaging model that can account for blur. Lastly, Sect. V reports physics-informed reconstructions of underexpanded jets and Sect. VI recaps our conclusions and relates our plans for future work.

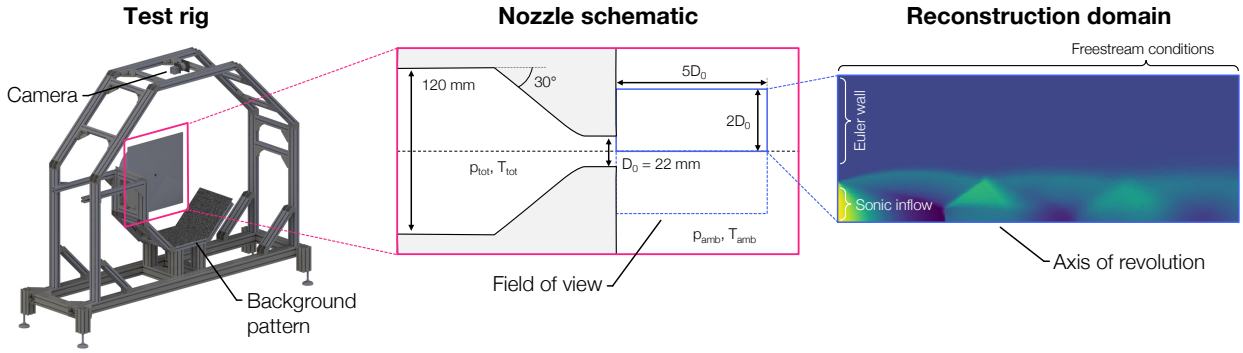

Fig. 1 Facility (left), nozzle schematic (middle), and reconstruction domain (right) for BOS tests of underexpanded jets. Pressurized air flows through a convergent nozzle and exits at sonic conditions. A camera is focused through the jet onto a background pattern to record BOS images.

II. Physics-Informed BOS for Turbulent Flows

Physics-informed neural networks can be used to solve a wide variety of forward and inverse problems that are governed by differential equations [15–18]. Here, we focus on the use of PINNs to learn turbulent mean fields with a RANS model. Notably, this has only been done for incompressible flows up until now. A summary of RANS-based PINNs is provided in Appendix A. Below, we introduce PINNs for physics-informed BOS and discuss the basics of our measurement models.

A. Physics-informed reconstruction

An overview of physics-informed BOS is illustrated in Fig. 2. Per the diagram, we directly reconstruct the axisymmetric density, ρ; velocity, u and v; total energy, E; and eddy viscosity, μ_T, fields from BOS data with a

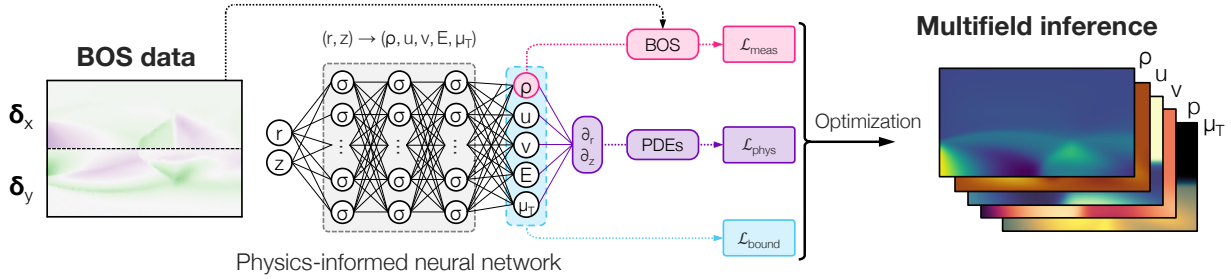

Fig. 2 PINNs are used to map axial and radial coordinates to flow fields. A BOS measurement model is included in $\mathcal{L}_{\text{meas}}$; the compressible RANS equations are in $\mathcal{L}_{\text{phys}}$; and experimental jet exit and boundary conditions are weakly imposed via $\mathcal{L}_{\text{bound}}$.

PINN. The network serves as a functional representation of the flow, mapping spatial coordinates to physical outputs, $(r, z) \rightarrow (\rho, u, v, E, \mu_{\text{T}})$, and is trained to minimize an objective loss that comprises measurement, physics, and boundary loss components:

$$\mathcal{L}_{\text{total}} = \omega_{\text{meas}}\,\mathcal{L}_{\text{meas}} + \omega_{\text{phys}}\,\mathcal{L}_{\text{phys}} + \omega_{\text{bound}}\,\mathcal{L}_{\text{bound}}. \tag{1}$$

In this expression, the ω terms are used to weight the influence of each loss component on $\mathcal{L}_{\text{total}}$. The measurement loss compares experimental BOS images or deflection data to synthetic measurements from the PINN. Synthetic data are produced with a measurement model that is described in the next section. The boundary loss includes reference values like known inflow conditions, and the physics loss is computed by plugging partial derivatives of the PINN into the governing equations. This is often done via automatic differentiation, which can be used to take partials of the network's outputs with respect to its inputs, denoted u_z, v_r, etc. By minimizing $\mathcal{L}_{\text{total}}$, the PINN approximately satisfies the governing equations and replicates any measurements included in $\mathcal{L}_{\text{meas}}$.

We previously used the compressible Euler equations to learn axisymmetric and planar inviscid flows [14]. The Euler equations were augmented with an irrotationality equation, which was expected to hold for the cone shock and expansion fan considered in [14]. Including redundant physical constraints in this manner can significantly improve the accuracy of reconstructions in the presence of noise or blur. Additionally, while we found that the dimensional and non-dimensional Euler equations, alike, could be successfully solved via $\mathcal{L}_{\text{phys}}$, the non-dimensional form provided additional stability. In this work, we utilize the non-dimensional compressible RANS equations, which are provided in Appendix B. The physics loss (Eq. (14) in Appendix B) is constructed by integrating residuals from the governing equations throughout the measurement domain, which has length $L = 5D_0$ and radius $R = 2D_0$, using the Monte Carlo method.

Boundary conditions may also be employed to mitigate the effects of weak solutions. Inflow conditions are generally known to first order for experiments like our underexpanded jet tests (described in Sect. III). Here, a jet exit condition is specified for ρ, u, v, and E in the core of the nozzle (i.e., at the $z = 0$ plane) from the axis of symmetry up to $r = D_0/4$. Flow in this region is expected to exhibit a flat profile and be sonic because the nozzle is choked. We do not set an inlet condition for μ_{T}. An Euler wall is positioned along the $z = 0$ plane from $r = D_0/2$ to R. This condition corresponds to the baseplate shown in Fig. 1. Along the top of the reconstruction domain, from $z = 0$ to L at $r = R$, all fields are set to the ambient conditions. This equality is weakly enforced. By contrast, hard positivity constraints are imposed on the axial velocity, total energy, and eddy viscosity fields by wrapping the corresponding network outputs in a softmax or exponential function.

B. Measurement Models

In BOS, refraction results in the "apparent motion" of the background pattern, which is quantified through the use of a computer vision algorithm like optical flow. This information is then reconstructed by inverting a discrete model of refraction. In physics-informed BOS, the inversion occurs implicitly by minimizing $\mathcal{L}_{\text{meas}}$, which contains the forward deflection model. Optical flow, a continuous model of refraction, and discrete models suitable for inversion are discussed below in that order.

1. Optical Flow

We use *optical flow* to determine the magnitude and orientation of deflections from a pair of reference and distorted images. This technique assumes that the brightness of features is conserved across the image pairs [19],

$$I(x, y, t) = I\big(x + \delta_\mathrm{x}, y + \delta_\mathrm{y}, t + \delta_\mathrm{t}\big)\,. \tag{2}$$

Here, I is the intensity of an image at the sensor position (x, y) and time t. The left side of Eq. (2) corresponds to the reference image while the right side describes an intensity field distorted by deflections, $\boldsymbol{\delta} = [\delta_\mathrm{x}, \delta_\mathrm{y}]^\mathrm{T}$, effectively warping the reference image. In principle, the intensity and deflection fields are continuous; in practice, they are discrete and are generally resolved at pixel centroids. The time between images, δ_t, is arbitrary in BOS and may be set to unity for convenience. Lastly, in the context of BOS, it is commonly assumed that changes in the scene are due strictly to refraction, as opposed to motion, shadows, reflections, and the like. Hence, variable illumination, motion, and light scattering off vapor are common sources of error in estimates of $\boldsymbol{\delta}$.

When deflections are small, Eq. (2) can be approximated with a first-order Taylor-series expansion,

$$I(x, y, t) \approx I(x, y, t) + I_x\,\delta_\mathrm{x} + I_y\,\delta_\mathrm{y} + I_t\,\delta_\mathrm{t}, \tag{3}$$

where I_x, I_y, and I_t are partial derivatives of the reference image with respect to x, y, and t. Setting δ_t to one yields the gradient-based optical flow equation,

$$I_x\,\delta_\mathrm{x} + I_y\,\delta_\mathrm{y} = -I_t, \tag{4}$$

Writing out Eq. (2) or (4) for each pixel produces an underdetermined system of equations having two unknowns for each equation: δ_x and δ_y. Numerous closures have been developed for optical flow, the most popular of which are the Horn–Schunck [20] and Lucas–Kanade [21] variants. Gradient-based optical flow can also be used to formulate a linear unified measurement model for BOS, in which the density field is directly related to image difference data through a matrix equation [22].

Most of the BOS scenarios considered in this work feature very large deflections, on the order of 10 px, invalidating the Taylor series expansion of Eq. (2). Consequently, gradient-based optical flow cannot be used for deflection sensing and unified BOS cannot be used in $\mathcal{L}_\mathrm{meas}$.* We thus use deflection data instead of raw image differences in this work. Deflections are estimated using ONERA's FOLKI algorithm [23], which is a nonlinear variant of Lucas–Kanade optical flow that is designed to accommodate large deflections and noisy images. The algorithm employs a coarse-to-fine multi-resolution scheme with Gaussian pyramids for interpolation. Optimization is conducted with a Gauss–Newton algorithm that has been tailored to run on a graphics processing unit (GPU). We use 11×11 px interrogation windows and estimate a displacement vector at each pixel.

Deflections are computed at each frame of the flow-on image set and then averaged to obtain mean data. The mean axial deflections exhibit a spurious trend, namely, a non-zero bias that increases with z, denoted $\varepsilon_{\delta_\mathrm{x}}$. This error is roughly constant at each axial slice, so we estimate $\varepsilon_{\delta_\mathrm{x}}$ using the top 200 rows of deflection data (i.e., outside the jet) and subtract this component off of δ_x.

2. Modeling Refraction with Depth of Field Effects

Visible distortions of the background pattern in BOS arise when wavefronts of light bend across refractive index gradients. The speed of a light in a gas of uniform composition is a linear function of the local molecular density, as codified by the Gladstone–Dale equation [24]. In the limit of geometric optics, the propagation of light can be approximated by infinitessimal "rays" that travel normal to phase fronts of the light wave, and refraction may be modeled in terms of a path integral along a ray [25],

$$\delta_\alpha = C_\mathrm{sys} \int_\mathrm{ray} \nabla_\alpha\,\rho(s)\,\mathrm{d}s, \tag{5}$$

for $\alpha \in \{x, y\}$, where ∇_α is the α-direction gradient operator and s is a progress variable that denotes the distance along the ray. The system constant C_sys, defined in [14], includes the Gladstone–Dale constant, lens magnification, physical size of the pixels, and distance from the flow to the background.

Equation (5) does not necessarily correspond to the signal recorded at a pixel. A real, finite aperture accepts a bundle of rays that may experience unique refractive index gradients. The whole bundle must be simulated to properly

*A nonlinear variant of unified BOS can be used for time- and scale-resolved reconstructions, but the linear technique is required to reconstruct mean fields from mean data.

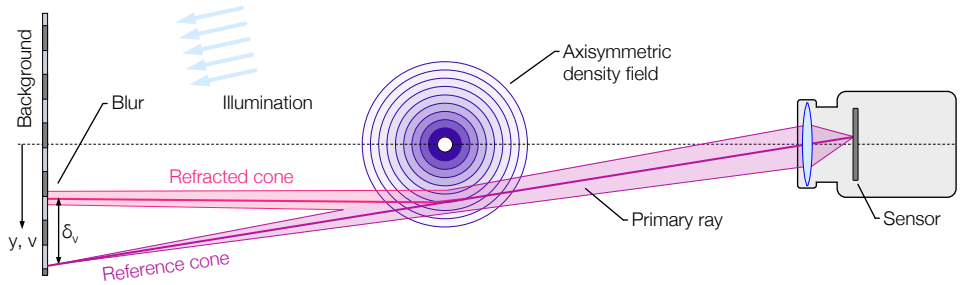

Fig. 3 Ray diagram of a BOS measurement that accounts for depth-of-field and blur. In the flow off condition, cones of light focus to a point on the background plate. Differential refraction through the flow causes blur in the flow-on images. Diagram is not to scale.

account for a finite depth-of-field and any resulting blur in BOS [26]. Cook and Porter [27] laid out a strategy to do this called "aperture sampling". This strategy is depicted in Fig. 3, where the light collected by a pixel comes from the cone centered around that pixel's primary ray; the cone has a base that is coincident with the camera's aperture and a diameter of $D_{\text{cone}} = f/f_\#$, where f is the focal length of the lens and $f_\#$ is the f-number. The cone's apex is given by the location of the pixel's primary ray in the camera's focal plane. Imaging is simulated as follows:

1) Individual rays are drawn at random from the cone,
2) ray tracing is conducted for each sample, from the camera to the background, and
3) the resulting intensities are averaged.

In BOS, this means that linear or nonlinear ray-tracing must be used to determine the deflection of each ray from the conical bundle in the plane of the background pattern. Linear ray-tracing is sufficient for small deflections whereas a nonlinear technique must be employed in the presence of large cumulative refractive index gradients.

3. Discrete Deflectometry Models

The continuous model in Eq. (5) is discretized to simulate deflection measurements for an arbitrary density field, often called a "deflectometry" operator. We use a dense basis that is linear in r and uniform in z to discretize Eq. (5). Sipkens et al. [28] derived radial and axial deflectometry matrices for arbitrary rays supported by this basis, denoted $\mathbf{D}_\text{x}$ and $\mathbf{D}_\text{y}$ assuming that the x and y camera coordinates are aligned with the z-direction and r-direction in the midplane, respectively. The deflectometry system is

$$\boldsymbol{\delta}_\alpha = C_\text{sys}\,\mathbf{D}_\alpha \boldsymbol{\rho}, \tag{6}$$

where $\boldsymbol{\delta}_\alpha$ is a vector of α-direction deflections and $\boldsymbol{\rho}$ is a discrete representation of the density field. However, we note that this matrix is usually specified for infinitesimal rays. Therefore, we sample rows of $\mathbf{D}_\alpha$ from the corresponding cones of light to build an operator that accounts for depth-of-field effects. For each row, we sample a large number of rays from the matching cone, per the description in the previous section. We then average the sampled sensitivities. The resulting model applies to mean deflections as well as mean intensity differences in the linear regime of optical flow.

When processing deflection data, a measurement loss is specified using Eq. (6),

$$\mathcal{L}_\text{meas} = \left\| C_\text{sys}\,\mathbf{D}_\text{x}\boldsymbol{\rho} - \boldsymbol{\delta}_\text{x} \right\|_2^2 + \left\| C_\text{sys}\,\mathbf{D}_\text{y}\boldsymbol{\rho} - \boldsymbol{\delta}_\text{y} \right\|_2^2, \tag{7}$$

where $\boldsymbol{\rho}$ is a vector of density data outputted by the PINN and $\boldsymbol{\delta}_\text{x}$ and $\boldsymbol{\delta}_\text{y}$ contain mean axial and radial deflections, respectively, e.g., obtained via FOLKI in this paper. Note that the PINN yields normalized values of ρ so the outputted density field must be multiplied by ρ_0 (the jet exit density, in our case) to populate $\boldsymbol{\rho}$.

One way to improve BOS is to use a unified operator to eliminate the deflection sensing step [22]. When processing mean fields, this requires deflections to be on the order of 1 px to remain in the linear regime. This criterion can be guaranteed by a careful experimental design, e.g., setting an appropriate object-to-background distance and selecting a pattern with full-field gradients, like the sine waves in [14, 22]. In unified BOS, Eq. (3) is expressed in matrix form for the whole set of pixels. The horizontal and vertical intensity gradients are stored in diagonal matrices with elements $\mathbf{X}_{i,i} = I_{x,i}$ and $\mathbf{Y}_{i,i} = I_{y,i}$, respectively. Next, a data vector is constructed directly from the image pair, $\mathbf{b} = \{-I_{t,i}\}_{i=1}^m$ for a system of m pixels. Lastly, the x- and y-direction instances of Eq. (6) are substituted in place of $\boldsymbol{\delta}_\text{x}$ and $\boldsymbol{\delta}_\text{y}$ to relate

the image data to the density field,

$$\mathbf{X}\boldsymbol{\delta}_\mathrm{x} + \mathbf{Y}\boldsymbol{\delta}_\mathrm{y} = C_\mathrm{sys}\left(\mathbf{X}\mathbf{D}_\mathrm{x} + \mathbf{Y}\mathbf{D}_\mathrm{y}\right)\boldsymbol{\rho} = \mathbf{b}. \tag{8}$$

This equation can be leveraged to specify an image difference-based measurement loss,

$$\mathcal{L}_\mathrm{meas} = \left\| C_\mathrm{sys}\left(\mathbf{X}\mathbf{D}_\mathrm{x} + \mathbf{Y}\mathbf{D}_\mathrm{y}\right)\boldsymbol{\rho} - \mathbf{b}\right\|_2^2. \tag{9}$$

We previously used this model to reconstruct inviscid supersonic flows [14]. However, for reasons detailed in Sect. II.B.1, unified BOS could not be applied in the present case.

III. Measurement Scenario

A. Underexpanded Jets

Underexpanded jets may be characterized in terms of their nozzle pressure ratio (NPR), which describes the ratio of total pressure, p_tot, to ambient pressure, p_amb. This value is directly related to the exit Mach number that would be reached at the same initial conditions if said jet was fully expanded,

$$M_\mathrm{jet} = \sqrt{\frac{2}{\gamma - 1}\left(\mathrm{NPR}^{\frac{\gamma-1}{\gamma}} - 1\right)}, \tag{10}$$

called the fully expanded jet Mach number. The fully expanded *density* is another useful metric for assessing the expansion of a jet [29],

$$\rho_\mathrm{jet} = \frac{p_\mathrm{tot}}{R_\mathrm{gas}\, T_\mathrm{tot}}\mathrm{NPR}^{-1/\gamma}, \tag{11}$$

where R_gas is the gas constant. As the jet expands, the centerline density should converge to this value. Oftentimes, density is normalized by ρ_jet when plotted, such that the trace asymptotes to one.

At sufficiently high NPRs, significant flow structures arise, some of which are visible in the density field depicted in Fig. 1. Firstly, density decreases when the flow exits the nozzle because the exit pressure is larger than the ambient pressure. An expansion fan forms immediately at the nozzle's outlet, delimited by a structure known as a barrel shock. The diamond shock cells seen in Fig. 1 are characteristic of imperfectly expanded jets and are formed by an oblique shocks paired with an expansion fan. Successive normal shocks along the centerline, called Mach disks, correspond to strong compressions of the flow. Notably, the region immediately following a Mach disk is subsonic while the surrounding flow remains supersonic. These phenomena can be difficult to capture experimentally as well as computationally.

Instabilities in underexpanded jets can produce aero-acoustic effects like screech noise through a variety of complex mechanisms [30]. For example, Kelvin–Helmholtz instabilities can interact with shock cells to generate acoustic waves, which have been the subject of numerous experimental and theoretical campaigns, as reviewed by Seiner [31] and Raman [32]. These features have also been studied computationally, e.g., by Maté et al. [33], Rona and Zhang [34], and Lehnasch and Bruel [35]. Additional phenomenalogical descriptions about the specific jets considered in this work can be found in the text of Nicolas et al. [36].

B. BOS Measurements

Experiments reported in this paper were performed at ONERA in Toulouse, France. A complete description of the facility is provided in [36]. It consists of a $D_0 = 22$ mm convergent nozzle, fed by an air tank that is regulated at 20 °C by a 570 kW heater to prevent condensation. The nozzle continually converges to ensure a sonic condition at the outlet. We consider NPRs of 3, 4, and 5, corresponding to $M_\mathrm{jet} = 1.36$, 1.56, and 1.71, respectively.

The data set for each test consists of 900 images, recorded at 10 Hz. Imaging is conducted with a JAI BM-500GE camera having a 5 MP sensor and 3.45 µm pixels. The camera is equipped with a 70 mm lens and mounted at a distance of 1 m from the jet centerline on the hexagonal test bench depicted in Fig. 1. The field of view covers $5D_0$ axially and $4D_0$ radially. A patterned background is placed opposite the camera at a distance of 0.4 m from the jet's central axis. The pattern consists of dots of diameter 0.2 mm (approximately 3 px); the dots placed in a semi-random manner to fill the space. Nicolas et al. [37] determined this background to be more resilient for deflection sensing in a harsh environment than purely random dots or a wavelet background.

Illumination is provided by a Quantel Twins BSL double-pulsed laser. Both pulses fire during the camera's exposure to maximize the intensity of illumination. Light from the lasers is spread onto the background using 50 mm lenses. However, the amount of light received by the camera is only sufficient to operate at an f-number of eight. Nicolas et al. [36] determined this aperture setting to be a sub-optimal as it corresponds to a relatively large circle of confusion in the measurement volume, measuring about 2.5 mm in diameter or $0.11D_0$. In Sect. IV, we demonstrate how blur can be modeled by aperture sampling to improve the accuracy of reconstructions for such a setup.

C. CFD Study

A delayed detached eddy simulation of the most underexpanded jet (NPR = 5) is conducted for comparison. We perform the simulation in FLUENT 14, using a domain size of $25D_0$ axially and $20D_0$ radially. The pipe flow upstream of the nozzle is included as part of the simulation, with a $20D_0$ domain leading up to the exit plane. The grid consists of around 10 million cells; a second-order upwind spatial scheme and second-order implicit temporal scheme are employed to solve the governing equations, using the advection upstream splitting method for flux calculations. Flow is simulated via the classical Smagorinsky and Spalart–Allmaras closures; a RANS treatment is applied inside the pipe and the solver imposes a modified length scale to ensure RANS calculations throughout the boundary layer, as well. Total pressure and temperature are applied at the inlet, with an atmospheric pressure condition and turbulence level of 5%. While this simulation is somewhat under-resolved in the downstream region, it provides sufficient qualitative accuracy to benchmark our physics-informed BOS results.

IV. Analysis of Blur Effects

It is important to use a forward operator that properly captures the imaging physics in BOS data assimilation. However, to the best of our knowledge, all BOS algorithms reported to date assume thin rays, corresponding to a pinhole camera model. This model is known to break down for large apertures and strong refractive index gradients, especially those produced by compressible flow features like a shock or expansion fan. An open aperture yields large cones of light that may span a range of gradients, leading to blurry images and damped deflections [38, 39]. Here, we analyze the effects of primary ray versus cone ray models for BOS.

We simulate deflections for our experimental setup using the CFD-based NPR5 density field shown in Fig. 4. The left most deflection panels depict the axial and radial components of deflections for a pinhole camera, i.e., using only the principal ray of each pixel to construct $\mathbf{D}_x$ and $\mathbf{D}_y$. This calculation predicts massive deflections near the shocks, with magnitudes up to 20 px. Cone ray deflections obtained via aperture sampled operators are shown in the central column. We built operators with up to 500 samples per cone and observed reliable convergence at around 50 samples. Cone ray deflections are smaller and smoother than primary ray deflections, resulting in blurrier flow structures. In the final column, we show mean deflections from the FOLKI algorithm, which are qualitatively similar to the aperture sampled results. However, it should be noted that the synthetic cone deflections are both larger than the FOLKI estimates and feature sharper flow structures.

To understand the discrepancy between our measured and modeled deflections, we simulate the mean flow-on image via nonlinear aperture sampling. Our simulation includes 500 random rays per cone, which are propagated through the CFD density field for an NPR5 jet by nonlinear ray tracing. The intensity of each ray is calculated via bilinear

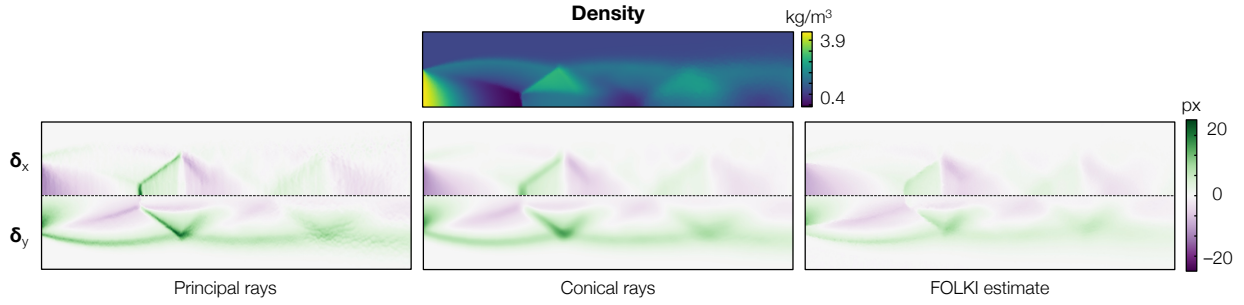

Fig. 4 Synthetic deflections calculated for a CFD-based density field (top) using a pinhole camera model (left) and cone beam rays (middle). Also shown are experimental deflections from the FOLKI algorithm (right).

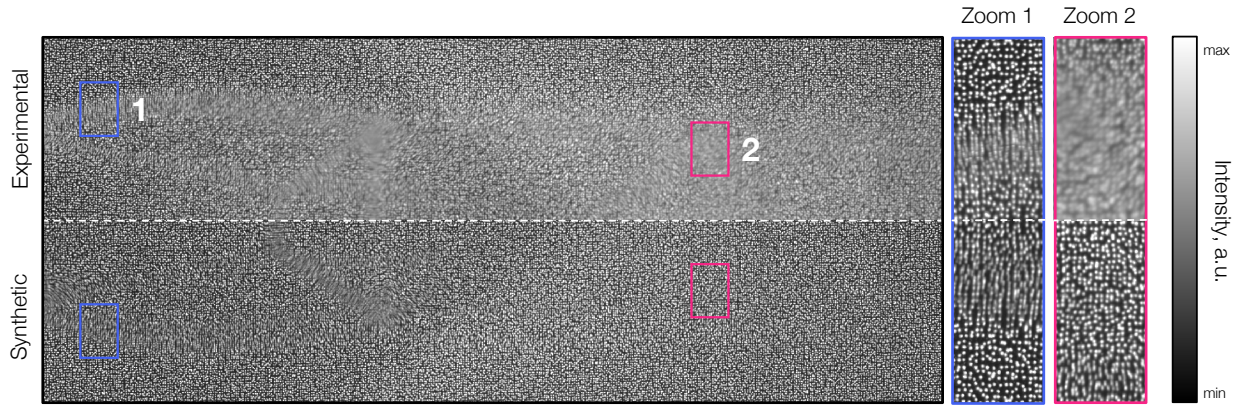

Fig. 5 Mean experimental flow-on image for the NPR5 jet and a synthetic image based on the mean CFD density field. The nonlinear model captures blur in steady regions (blue) but not in turbulent regions (fuchsia).

interpolation of the experimental reference image at the deflected location, and the intensity of a pixel is simply the average for the cone. Note that this model is nonlinear so the mean distorted image for a turbulent flow is not generally equal to the image computed using the mean density field. Results of this simulation are shown in Fig. 5, which includes the mean experimental flow-on image and our simulation based on the mean density field. Two zoom regions are depicted on the right side of the figure: one upstream of the first Mach disk (blue border) and the other close to the second Mach disk (fuchsia border). Blur in the first instance is well captured by our model; notably, this is a region with large deflections and appreciable blur, which cannot be simulated with a pinhole camera. However, we are unable to mimic the experimental image in the downstream region.

Experimental and synthetic images in the second zoom box in Fig. 5 are emblematic of downstream conditions. The experimental image appears to be far blurrier and slightly brighter than the synthetic image. There are two key effects at play, here. First, the imaging model is nonlinear and projections of the mean density field will not necessarily capture the mean intensity field in regions that sustain turbulent fluctuations. Indeed, extraneous blur is concentrated in regions where the flow is known to be turbulent. This effect could be mitigated by tailoring the test setup to satisfy the assumptions of linear optical flow. Second, the experimental flow-on images are brighter than than the reference images. We observe this effect by comparing the intensity histogram of the image sets, i.e., the flow-on distribution is brighter than the flow-off distribution. Increased brightness could be due to light scattering off condensation, in principle, but the location of "surplus" brightness is inconsistent with this explanation because condensation would be concentrated at the nozzle outlet. Hence, we currently lack a satisfactory explanation for this phenomenon.

V. BOS–RANS Data Assimilation for Underexpanded Jets

We process mean deflections from FOLKI to reconstruct underexpanded jets with an NPR of 3, 4, and 5, using a PINN with the compressible RANS equations to determine the mean flow fields. These PINNs are implemented in TensorFlow 2.9.2 and consist of 10 hidden layers, each having 50 nodes per output. Weights are randomly initialized with a standard normal distribution and the biases start off at zero. Training is conducted with the Adam optimizer using a learning rate of 10^{-3} for 10 epochs followed by a rate of 10^{-4} for another 10 epochs, which is sufficient for convergence. We use data, physics, and boundary batch sizes of 500 pixels, 1000 interior points, and 300 boundary points, respectively. Figure 6 depicts the mean density, velocity, and pressure field of all three jets as well as the CFD solution for the NPR5 case.

Our physics-informed BOS estimates closely match the CFD results, both qualitatively and quantitatively, demonstrating that rich information about a compressible flow is accessible from BOS measurements via data assimilation. We observe subsonic flow after the Mach disk as well as successive expansion fans and oblique shock waves along the jet. However, we also note the presence of a couple artifacts. Namely, compression at the Mach disks is too gradual and velocity appears to be underpredicted in the outer shear layer. The CFD grid coarsens downstream, which could explain some of the discrepancies observed towards the edge of the jet. That said, the velocity errors could also originate with the eddy viscosity field, which is currently utilized by the PINN to compensate for errors in the deflection data.

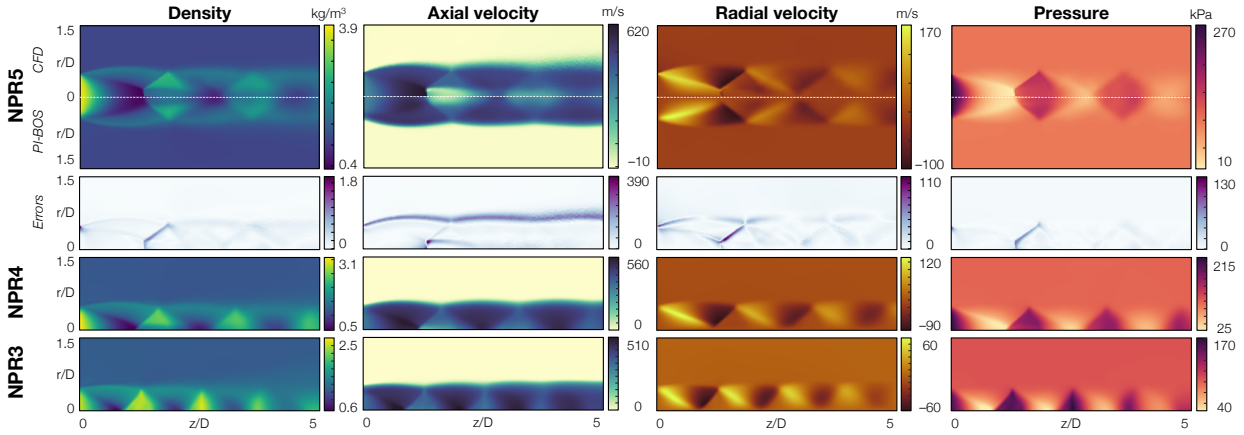

Fig. 6 Physics-informed reconstructions of underexpanded jets (NPR = 3, 4, and 5) from experimental BOS measurements. CFD results are shown for the most underexpanded jet. All of our reconstructed NPR5 fields bear a close resemblance to the CFD solution.

Readers should note that we infer μ_T without any structure from a turbulence model. Including a Spalart–Allmaras, SST k–ω, or other model and floating key parameters for model calibration or adding a corrective force [40] could potentially improve the accuracy of reconstructions and guide model development. A detailed analysis of the eddy viscosity fields produced by our DA scheme is forthcoming. We will report and analyze the Reynolds stresses implied by our reconstructions and compare them to modeled fields.

For the NPR5 case, deflection data in the immediate vicinity of the first Mach disk is neglected. We previously found that it is beneficial to ignore measurements in regions of the flow that produce very large deflections, including shock fronts and expansion corners, which correspond to singularities in the Euler equations [14]. The paraxial assumption, used to derive the linear deflectometry operator, breaks down in these regions, leading to model errors and spurious inferred flow features. Moreover, deflection sensing is particularly difficult in the presence of blur, which is acute about the Mach disk. In separate tests, we included all the deflection data in our training set, but doing so smeared the first Mach disk slightly more than our current set. The latent fields are also adversely affected by the near-disk deflections: the subsonic region recedes downstream, corresponding to larger physics residuals. Crucially, in previous work, we found that it is difficult to counteract noisy measurements by adjusting the relative weight of $\mathcal{L}_{\text{meas}}$ and $\mathcal{L}_{\text{phys}}$ [41]. Instead, errors in the deflection data must be modeled and discounted accordingly.

We do not have CFD fields to validate the NPR3 and NPR4 reconstructions in Fig. 6. Nevertheless, based on our NPR5 results, we are confident in the quality of our lower-NPR reconstructions. Further, we find that the flow structures are comparable to previous reconstructions [36] and the latent fields agree with our physical intuition about the jets. We also note that the mean shock locations and spacing in our reconstructions are consonant with results available in literature [42, 43]. To demonstrate this, Fig. 7 depicts cut-plots of density along the the symmetry line from our physics-informed reconstructions, previous tomographic estimates [36], and our CFD prediction for the NPR5 jet. Density is normalized by the fully expanded value and plotted as a function of streamwise distance. We find that our physics-informed BOS results are similar to the 12-view tomographic BOS reconstructions of Nicolas et al. [36]. The latter fields constitute the azimuthal average of a non-axisymmetric reconstruction, which may explain some of the minor differences.

VI. Conclusions and Outlook

This work demonstrates the application of physics-informed BOS to turbulent underexpanded jets. Our approach incorporates an aperture-dependent measurement model and the compressible RANS equations to infer mean density, velocity, energy, and eddy viscosity fields from deflection data. We use a physics-informed neural network to represent the flow; "PINNs" are flexible tools for data assimilation and we have previously used them to reconstruct inviscid, supersonic flow from noisy experimental images. To the best of our knowledge, this work reports the first usage of PINNs to reconstruct a turbulent, compressible flow using the full RANS equations. We report accurate, multi-parameter reconstructions that are produced without an explicit turbulence model, although we do invoke the

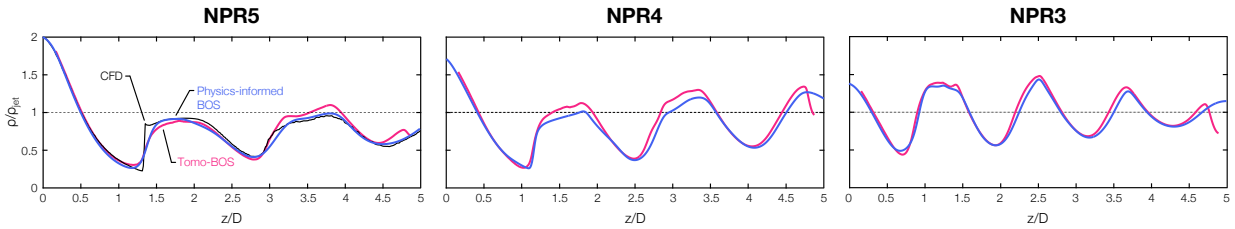

Fig. 7 Normalized axial density distributions for the NPR5 (left), NPR4 (middle) and NPR3 (right) jets. Physics-informed BOS results are shown in blue, 12-view tomographic BOS results from [36] are plotted in fuchsia, and CFD results for the NRP5 jet are drawn in black.

Boussinesq approximation. Future work will incorporate such models, allowing for the direct calibration and inference of model-form errors from experimental measurements.

Three important conclusions can be drawn from this work.

1) Physics-informed BOS with a PINN yields accurate estimates of the density fields, commensurate with previous reconstructions produced with the same deflection data. Additionally, there is good agreement amongst the velocity and pressure fields inferred from BOS data and produced by a CFD simulation. This behavior tracks to experimental cases without CFD validation, wherein the inferred velocity and pressure fields agree with engineering intuition.
2) Reconstructions are susceptible to errors that stem from the deflection sensing step. Therefore, to minimize artifacts and recover sharp flow structures, we recommend starting with raw image data and utilizing a unified BOS measurement model.
3) Blur effects are non-negligible in imaging scenarios with large density gradients, leading to large deviations between the deflections computed with a pinhole model and those from a cone ray model. A measurement model that incorporates cone ray sensitivities is developed and demonstrated for use in BOS experiments.

Appendix A. PINNs with the RANS Equations

Several groups have implemented PINNs with a RANS model. For instance, Eivazi et al. [44] solved four forward problems with a RANS-PINN: zero and adverse pressure gradient boundary layers, flow over a NACA airfoil, and flow over a periodic hill. The authors inferred Reynolds stress fields from rich boundary data (i.e., a dense string of colocation points) without using an explicit RANS model. In other words, the Reynolds stresses were underdetermined and implicitly regularized by the PINN. While this strategy was tractable in some scenarios – i.e., sans pressure gradients – the lack of closure led to large errors in the other flows. Separately, Xu and coworkers [45] considered steady and unsteady cases involving a backward facing step and flow past a cylinder, respectively. The authors outputted an *unmodeled* eddy viscosity field instead of inferring the full Reynolds stress tensor like Eivazi et al. We note that the mean fields were recovered to high accuracy, even in the presence of substantial noise, but the inferred distribution of eddy viscosity bore a minimal (in some cases negligible) resemblance to that of the ground truth CFD data, regardless of the underlying model: SST k–ω or SST-SAS, in this instance. Von Saldern et al. [46] also inferred the eddy viscosity as an additional latent field. They considered several targets, including a isothermal jet with and without swirl as well as a jet flame. The full RANS equations, simplified via the Boussinesq approximation, were used to model the swirling jet whereas the other flows were learned solely using the continuity or turbulent boundary layer equations.

While Eivazi [44], Xu [45], and their colleagues exclusively employed synthetic data, von Saldern [46] used both large-eddy simulations and particle image velocimetry measurements in their work. For this paper, we assimilated experimental BOS data and the compressible RANS equations. This likely represents the first effort to implement the Favre-averaged RANS equations in a PINN setting. The Boussinesq assumption is invoked and an eddy viscosity field is inferred such that our mean fields are trained to satisfy Eq. (13) in Appendix B.

Appendix B. Axisymmetric Compressible RANS Equations

Non-dimensional equations play an important role in stabilizing many CFD solvers. A similar phenomenon is observed in PINNs: scaling the components of each equation to order one leads to substantial improvements in the

stability of training [14, 47]. Here, we denote the non-dimensional quantities of interest using an asterisk, $(\cdot)^*$, i.e., ρ^* for density, u^* and v^* for velocity, etc. We non-dimensionalize these terms with a jet diameter length scale, D_0; outlet density, ρ_0; outflow velocity, u_0; settling chamber temperature, T_0; and viscosity similarly given by the settling chamber conditions, μ_0. Pressure is non-dimensionalized in terms of the density and velocity scales. Dimensional quantities correspond to the product of a non-dimensional variable and its scale: $\rho = \rho^* \rho_0$, $u = u^* u_0$, and so forth. The scales are arranged to form two important non-dimensional numbers that appear in the RANS equations, namely, a reference Reynolds number,

$$Re_0 = \frac{\rho_0 \, u_0 \, D_0}{\mu_0} \tag{12a}$$

and Mach number,

$$M_0 = \frac{u_0}{\sqrt{\gamma \, R_{\text{gas}} \, T_0}}. \tag{12b}$$

The equations also include Prandtl and turbulent Prandtl numbers, $Pr_0 = 0.72$ and $Pr_\text{T} = 0.9$, respectively, which are assumed to be constant.

The non-dimensional, Favre-averaged continuity and Navier–Stokes equations are written as follows:

$$\varepsilon_1 = \frac{\partial}{\partial z^*}\left(\rho^* u^*\right) + \frac{1}{r^*}\frac{\partial}{\partial r^*}\left(r^* \rho^* v^*\right) \tag{13a}$$

$$\varepsilon_2 = \frac{\partial}{\partial z^*}\left(\rho^* u^{*2} + p^* - Re_0^{-1}\tau_{zz}^*\right) + \frac{1}{r^*}\frac{\partial}{\partial r^*}\left[r^*\left(\rho^* u^* v^* - Re_0^{-1}\tau_{zr}^*\right)\right] \tag{13b}$$

$$\varepsilon_3 = \frac{\partial}{\partial z^*}\left(\rho^* u^* v^* - Re_0^{-1}\tau_{rz}^*\right) + \frac{\partial}{\partial r^*}\left(\rho^* v^{*2} + p^* - Re_0^{-1}\tau_{rr}^*\right) + \frac{1}{r^*}\left[\rho^* v^{*2} - Re_0^{-1}\left(\tau_{rr}^* + \tau_{\theta\theta}^*\right)\right] \tag{13c}$$

$$\begin{aligned}\varepsilon_4 = {} & \frac{\partial}{\partial z^*}\left[\left(\rho^* E^* + p^*\right) u^* - Re_0^{-1}\left(\tau_{zz}^* u^* + \tau_{zr}^* v^*\right) - \frac{q_z^*}{(\gamma-1)\, M_0^2 Re_0}\right] + \\ & \frac{1}{r^*}\frac{\partial}{\partial r^*}\left\{r^*\left[\left(\rho^* E^* + p^*\right) v^* - Re_0^{-1}\left(\tau_{rr}^* v^* + \tau_{rz}^* u^*\right) - \frac{q_r^*}{(\gamma-1)\, M_0^2 Re_0}\right]\right\},\end{aligned} \tag{13d}$$

where ε_1–ε_4 are residuals. Our RANS physics loss is thus written as follows:

$$\mathcal{L}_\text{phys} = \frac{1}{\pi R^2 L}\int_0^L \int_0^R \|[\varepsilon_1, \ldots, \varepsilon_4]\|_2^2 \, 2\pi r \, \mathrm{d}r \, \mathrm{d}z. \tag{14}$$

The stress terms in Eq. (13) take the form presented in Eq. (15). Note that the total energy equation is written under the assumption that turbulent molecular diffusion and transport are negligible [48].

In this document, τ includes both the Reynolds-averaged viscous tensor components and the Reynolds stress tensor fluxes, the latter of which are modeled using a classical Boussinesq formulation for flows with non-zero divergence. Similarly, the heat fluxes, q_r and q_z, include both heat diffusion and modeled turbulent enthalpy fluxes, which are also closed via the Boussinesq formulation. We assume that the turbulent eddy viscosity, μ_T, is additive with molecular viscosity, μ, and incorporate μ_T into the second coefficient of viscosity. This allows for the viscous tensor terms to be represented as

$$\tau_{zz}^* = \left(\mu^* + \mu_\text{T}^*\right)\left[\frac{4}{3}\frac{\partial u^*}{\partial z^*} - \frac{2}{3}\left(\frac{\partial v^*}{\partial r^*} + \frac{v^*}{r^*}\right)\right] \tag{15a}$$

$$\tau_{zr}^* = \tau_{rz}^* = \left(\mu^* + \mu_\text{T}^*\right)\left(\frac{\partial u^*}{\partial r^*} + \frac{\partial v^*}{\partial z^*}\right) \tag{15b}$$

$$\tau_{rr}^* = \left(\mu^* + \mu_\text{T}^*\right)\left[\frac{4}{3}\frac{\partial v^*}{\partial r^*} - \frac{2}{3}\left(\frac{\partial u^*}{\partial z^*} + \frac{v^*}{r^*}\right)\right] \tag{15c}$$

$$\tau_{\theta\theta}^* = \left(\mu^* + \mu_\text{T}^*\right)\left[\frac{4}{3}\frac{v^*}{r^*} - \frac{2}{3}\left(\frac{\partial u^*}{\partial z^*} + \frac{\partial v^*}{\partial r^*}\right)\right] \tag{15d}$$

and the heat fluxes to be represented as

$$q_z^* = \left(\frac{\mu^*}{Pr_0} + \frac{\mu_T^*}{Pr_T} \right) \frac{\partial T^*}{\partial z^*} \tag{16a}$$

$$q_r^* = \left(\frac{\mu^*}{Pr_0} + \frac{\mu_T^*}{Pr_T} \right) \frac{\partial T^*}{\partial r^*}, \tag{16b}$$

where the gas constant for air is $R_{gas} = 287$ J kg^{-1} K^{-1} and the ratio of specific heats is assumed to be $\gamma = 1.4$. In this notation, turbulent kinetic energy, k – which is either modeled algebraically or solved as a control variable in a one- or two-equation turbulence model – is coupled to the momentum and energy equations through μ_T. The non-dimensional temperature is

$$T^* = \gamma \left(\gamma - 1 \right) M_0^2 \left[E^* - \frac{1}{2} \left(u^{*2} + v^{*2} \right) \right], \tag{17}$$

and the non-dimensional pressure may be computed via a dimensionless equation of state,

$$p^* = \frac{\rho^* T^*}{\gamma M_0^2}. \tag{18}$$

Similarly, non-dimensional viscosity may be calculated from the temperature via a non-dimensional version of Sutherland's formula,

$$\mu^* = \frac{C_1 T_0^{1/2}}{\mu_0} \left(\frac{T^{*3/2}}{T^* + S/T_0} \right). \tag{19}$$

We use the two-constant form of this equation, with $C_1 = 1.458 \times 10^{-6}$ kg m^{-1} s^{-1} K$^{-1/2}$ and $S = 110.4$ K.

Acknowledgments

This material is based upon work supported by the National Science Foundation under Grant No. 2227763, the Erlangen Graduate School in Advanced Optical Technologies at the Friedrich-Alexander-Universität Erlangen-Nürnberg, and a Department of Defense National Defense Science and Engineering Graduate Fellowship.

References

[1] Bush, R. H., Chyczewski, T. S., Duraisamy, K., Eisfeld, B., Rumsey, C. L., and Smith, B. R., "Recommendations for future efforts in RANS modeling and simulation," *AIAA SciTech 2019 Forum*, 2019, p. 0317.

[2] Pope, S. B., *Turbulent Flows*, Cambridge University Press, 2000.

[3] Ben Ali, M. Y., Léon, O., Donjat, D., Bézard, H., Laroche, E., Mons, V., and Champagnat, F., "Data assimilation for aerothermal mean flow reconstruction using aero-optical observations: a synthetic investigation," *56th 3AF International Conference on Applied Aerodynamics*, 2022, pp. 1–17.

[4] Dolvin, D., "Hypersonic international flight research and experimentation (HIFiRE) fundamental science and technology development strategy," *15th AIAA International Space Planes and Hypersonic Systems and Technologies Conference*, 2008, p. 2581.

[5] Wall, A. T., Gee, K. L., Morris, P. J., Colonius, T., and Lowe, K. T., "Introduction to the special issue on supersonic jet noise," , 2022.

[6] Settles, G. S., and Hargather, M. J., "A review of recent developments in schlieren and shadowgraph techniques," *Meas. Sci. Technol.*, Vol. 28, No. 4, 2017, p. 042001.

[7] Hargather, M. J., and Settles, G. S., "A comparison of three quantitative schlieren techniques," *Opt. Lasers Eng.*, Vol. 50, No. 1, 2012, pp. 8–17.

[8] Kaipio, J., and Somersalo, E., *Statistical and Computational Inverse Problems*, Springer Science & Business Media, 2006.

[9] Schmidt, B. E., and Woike, M. R., "Wavelet-Based Optical Flow Analysis for Background-Oriented Schlieren Image Processing," *AIAA J.*, Vol. 59, No. 8, 2021, pp. 3209–3216.

[10] Grauer, S. J., Mohri, K., Yu, T., Liu, H., and Cai, W., "Volumetric emission tomography for combustion processes," *Prog. Energy Combust. Sci.*, Vol. 94, 2023, p. 101024.

[11] Elfving, T., Hansen, P. C., and Nikazad, T., "Semi-convergence properties of Kaczmarz's method," *Inverse Probl.*, Vol. 30, No. 5, 2014, p. 055007.

[12] Vauhkonen, M., Vadász, D., Karjalainen, P. A., Somersalo, E., and Kaipio, J. P., "Tikhonov regularization and prior information in electrical impedance tomography," *IEEE Trans. Med. Imaging*, Vol. 17, No. 2, 1998, pp. 285–293.

[13] Kolehmainen, V., Somersalo, E., Vauhkonen, P. J., Vauhkonen, M., and Kaipio, J. P., "A Bayesian approach and total variation priors in 3D electrical impedance tomography," *Proceedings of the 20th Annual International Conference of the IEEE Engineering in Medicine and Biology Society.*, Vol. 2, IEEE, 1998, pp. 1028–1031.

[14] Molnar, J. P., Venkatakrishnan, L., Schmidt, B. E., Sipkens, T. A., and Grauer, S. J., "Estimating density, velocity, and pressure fields in supersonic flow using physics-informed BOS," *arXiv preprint*, 2022, p. 2208.04280.

[15] Raissi, M., Perdikaris, P., and Karniadakis, G. E., "Physics-informed neural networks: A deep learning framework for solving forward and inverse problems involving nonlinear partial differential equations," *J. Comp. Phys.*, Vol. 378, 2019, pp. 686–707.

[16] Mao, Z., Jagtap, A. D., and Karniadakis, G. E., "Physics-informed neural networks for high-speed flows," *Comput. Methods Appl. Mech. Eng.*, Vol. 360, 2020, p. 112789.

[17] Cai, S., Wang, Z., Fuest, F., Jeon, Y. J., Gray, C., and Karniadakis, G. E., "Flow over an espresso cup: inferring 3-D velocity and pressure fields from tomographic background oriented Schlieren via physics-informed neural networks," *J. Fluid Mech.*, Vol. 915, 2021.

[18] Cai, S., Mao, Z., Wang, Z., Yin, M., and Karniadakis, G. E., "Physics-informed neural networks (PINNs) for fluid mechanics: A review," *Acta Mech. Sin.*, 2022, pp. 1–12.

[19] Davies, E. R., *Machine Vision: Theory, Algorithms, Practicalities*, Elsevier, 2004.

[20] Horn, B. K. P., and Schunck, B. G., "Determining optical flow," *Artif. Intell.*, Vol. 17, No. 1-3, 1981, pp. 185–203.

[21] Lucas, B. D., and Kanade, T., "An iterative image registration technique with an application to stereo vision," *Proceedings DARPA Image Understanding Workshop*, 1981, pp. 121–130.

[22] Grauer, S. J., and Steinberg, A. M., "Fast and robust volumetric refractive index measurement by unified background-oriented schlieren tomography," *Exp. Fluids*, Vol. 61, No. 3, 2020, pp. 1–17.

[23] Champagnat, F., Plyer, A., Le Besnerais, G., Leclaire, B., Davoust, S., and Le Sant, Y., "Fast and accurate PIV computation using highly parallel iterative correlation maximization," *Exp. Fluids*, Vol. 50, No. 4, 2011, pp. 1169–1182.

[24] Gardiner, Jr., W. C., Hidaka, Y., and Tanzawa, T., "Refractivity of combustion gases," *Combust. Flame*, Vol. 40, 1981, pp. 213–219.

[25] Stam, J., and Languénou, E., "Ray tracing in non-constant media," *Eurographics Workshop on Rendering Techniques*, Springer, 1996, pp. 225–234.

[26] Rajendran, L. K., Bane, S. P. M., and Vlachos, P. P., "PIV/BOS synthetic image generation in variable density environments for error analysis and experiment design," *Meas. Sci. Technol.*, Vol. 30, No. 8, 2019, p. 085302.

[27] Cook, R. L., Porter, T., and Carpenter, L., "Distributed ray tracing," *Proceedings of the 11th Annual Conference on Computer Graphics and Interactive Techniques*, 1984, pp. 137–145.

[28] Sipkens, T. A., Grauer, S. J., Steinberg, A. M., Rogak, S. N., and Kirchen, P., "New transform to project axisymmetric deflection fields along arbitrary rays," *Meas. Sci. Technol.*, Vol. 33, No. 3, 2022, p. 035201.

[29] Panda, J., and Seasholtz, R., "Measurement of shock structure and shock–vortex interaction in underexpanded jets using Rayleigh scattering," *Phys. Fluids*, Vol. 11, No. 12, 1999, pp. 3761–3777.

[30] Powell, A., "On the mechanism of choked jet noise," *Proc. Phys. Soc. London, Sect. B*, Vol. 66, No. 12, 1953, p. 1039.

[31] Seiner, J., "Advances in high speed jet aeroacoustics," *9th Aeroacoustics conference*, 1984, p. 2275.

[32] Raman, G., "Advances in understanding supersonic jet screech: review and perspective," *Prog. Aerosp. Sci.*, Vol. 34, No. 1-2, 1998, pp. 45–106.

[33] Maté, B., Graur, I. A., Elizarova, T., Chirokov, I., Tejeda, G., Fernández, J. M., and Montero, S., "Experimental and numerical investigation of an axisymmetric supersonic jet," *J. Fluid Mech.*, Vol. 426, 2001, pp. 177–197.

[34] Rona, A., and Zhang, X., "Time accurate numerical study of turbulent supersonic jets," *J. Sound Vib.*, Vol. 270, No. 1-2, 2004, pp. 297–321.

[35] Lehnasch, G., and Bruel, P., "A robust methodology for RANS simulations of highly underexpanded jets," *Int. J. Numer. Methods Fluids*, Vol. 56, No. 12, 2008, pp. 2179–2205.

[36] Nicolas, F., Donjat, D., Léon, O., Le Besnerais, G., Champagnat, F., and Micheli, F., "3D reconstruction of a compressible flow by synchronized multi-camera BOS," *Exp. Fluids*, Vol. 58, No. 5, 2017, pp. 1–15.

[37] Nicolas, F., Todoroff, V., Plyer, A., Le Besnerais, G., Donjat, D., Micheli, F., Champagnat, F., Cornic, P., and Le Sant, Y., "A direct approach for instantaneous 3D density field reconstruction from background-oriented schlieren (BOS) measurements," *Exp. Fluids*, Vol. 57, No. 1, 2016, pp. 1–21.

[38] Kirmse, T., Agocs, J., Schröder, A., Martinez Schramm, J., Karl, S., and Hannemann, K., "Application of particle image velocimetry and the background-oriented schlieren technique in the high-enthalpy shock tunnel Göttingen," *Shock Waves*, Vol. 21, No. 3, 2011, pp. 233–241.

[39] Elsinga, G. E., van Oudheusden, B. W., Scarano, F., and Watt, D. W., "Assessment and application of quantitative schlieren methods: Calibrated color schlieren and background oriented schlieren," *Exp. Fluids*, Vol. 36, No. 2, 2004, pp. 309–325.

[40] Rigas, G., Patel, Y., Marquet, O., and Mons, V., "Mean-flow reconstruction of unsteady flows via data assimilation: PINN vs variational methods," *Bull. Am. Phys. Soc.*, 2022.

[41] Molnar, J. P., and Grauer, S. J., "Flow field tomography with uncertainty quantification using a Bayesian physics-informed neural network," *Meas. Sci. Technol.*, Vol. 33, No. 5, 2022, p. 065305.

[42] Addy, A. L., "Effects of axisymmetric sonic nozzle geometry on Mach disk characteristics," *AIAA J.*, Vol. 19, No. 1, 1981, pp. 121–122.

[43] Lanzillotta, L., Léon, O., Donjat, D., and Le Besnerais, G., "3D density reconstruction of a screeching supersonic jet by synchronized multi-camera Background Oriented Schlieren," *EUCASS 2019*, 2019, pp. 1–15.

[44] Eivazi, H., Tahani, M., Schlatter, P., and Vinuesa, R., "Physics-informed neural networks for solving Reynolds-averaged Navier–Stokes equations," *Phys. Fluids*, Vol. 34, No. 7, 2022, p. 075117.

[45] Xu, H., Zhang, W., and Wang, Y., "Explore missing flow dynamics by physics-informed deep learning: The parameterized governing systems," *Phys. Fluids*, Vol. 33, No. 9, 2021, p. 095116.

[46] von Saldern, J. G., Reumschüssel, J. M., Kaiser, T. L., Sieber, M., and Oberleithner, K., "Mean flow data assimilation based on physics-informed neural networks," *Phys. Fluids*, Vol. 34, No. 11, 2022, p. 115129.

[47] Haghighat, E., Amini, D., and Juanes, R., "Physics-informed neural network simulation of multiphase poroelasticity using stress-split sequential training," *Comput. Methods Appl. Mech. Eng.*, Vol. 397, 2022, p. 115141.

[48] Rumsey, C., Smith, B., and Huang, G., "Description of a website resource for turbulence modeling verification and validation," *40th Fluid Dynamics Conference and Exhibit*, 2010, p. 4742.